

# DALI2: A NaI(Tl) detector array for measurements of $\gamma$ rays from fast nuclei

S. Takeuchi<sup>a,\*</sup>, T. Motobayashi<sup>a</sup>, Y. Togano<sup>b</sup>, M. Matsushita<sup>c</sup>, N. Aoi<sup>d</sup>, K. Demichi<sup>e</sup>, H. Hasegawa<sup>e</sup>, H. Murakami<sup>a</sup>

<sup>a</sup>RIKEN Nishina Center, Wako, Saitama 351-0198, Japan

<sup>b</sup>Department of Physics, Tokyo Institute of Technology, Meguro, Tokyo 152-8551, Japan

<sup>c</sup>CNS, University of Tokyo, RIKEN campus, Wako, Saitama 351-0198, Japan

<sup>d</sup>RCNP, Osaka University, Mihogaoka, Ibaraki, Osaka, 567-0047, Japan

<sup>e</sup>Department of Physics, Rikkyo University, Toshima, Tokyo 171-8501, Japan

---

## Abstract

A NaI(Tl) detector array called DALI2 (Detector Array for Low Intensity radiation 2) has been constructed for in-beam  $\gamma$ -ray spectroscopy experiments with fast radioactive isotope (RI) beams. It consists typically of 186 NaI(Tl) scintillators covering polar angles from  $\sim 15^\circ$  to  $\sim 160^\circ$  with an average angular resolution of  $6^\circ$  in full width at half maximum. Its high granularity (good angular resolution) enables Doppler-shift corrections that result in, for example, 10% energy resolution and 20% full-energy photopeak efficiency for 1-MeV  $\gamma$  rays emitted from fast-moving nuclei (velocities of  $v/c \simeq 0.6$ ). DALI2 has been employed successfully in numerous experiments using fast RI beams with velocities of  $v/c = 0.3 - 0.6$  provided by the RIKEN RI Beam Factory.

**Keywords:** Scintillation detector, In-beam  $\gamma$ -ray spectroscopy, Radioactive beam experiment

---

## 1. Introduction

The introduction of large arrays to  $\gamma$  detection systems for nuclear spectroscopy was primarily aimed at coping with heavy-ion induced reactions, which may produce cascades of  $\gamma$  rays containing multiple transitions. The Darmstadt-Heidelberg Crystal Ball, composed of 76 NaI(Tl) crystals, was a pioneering array developed in the 1980's [1]. Its ability to measure high-multiplicity events with high detection efficiency enabled the identification of states with higher spins compared to earlier studies that used conventional setups.

One direction of development was toward higher energy-resolution arrays by utilizing germanium (Ge) detectors [2–9]. GAMMASPHERE [2] and EUROBALL [3] are examples of large-scale arrays used in various spectroscopic experiments. Recent developments along this line are Ge tracking arrays such as GRETA [6, 7] and AGATA [9]. Another direction is toward higher efficiency measurements. The BaF<sub>2</sub>-crystal array was developed for astrophysical (n, $\gamma$ ) studies at Karlsruhe [10]. Another example CAESAR based on CsI(Na) scintillators is optimized for high  $\gamma$ -ray detection efficiency in in-beam  $\gamma$ -ray spectroscopy experiments at the National Superconducting Cyclotron Laboratory at Michigan State University [11]. For low-energy radioactive-beam experiments, the Miniball spectrometer using Ge detectors has been operational at REX-ISOLDE at CERN [12].

The recent development of fast radioactive ion beams requires a new type of  $\gamma$ -ray detector array for in-beam spectroscopic studies. Since experiments with such beams are performed in inverse kinematics where the  $\gamma$ -ray emitter has high

velocity, typically in the range  $v/c \simeq 0.3$  to 0.6, causing a large Doppler shift,  $\gamma$ -ray measurements require information on the direction of the radiation to extract the transition energy in the rest frame of the projectile. High efficiency is another requirement, since the secondary-beam intensity for nuclei far from stability is typically low. The CAESAR mentioned above is one of the arrays for such fast-beam applications. The RIKEN Radioactive Isotope Beam Factory (RIBF) [13] provides unique opportunities to research unstable nuclei owing to the production of the world's highest intensity exotic beams available today. To fully exploit the performance of the facility, we have built a new  $\gamma$ -ray detector array called DALI2. It consists of 186 NaI(Tl) crystals in its standard configuration, and has a reasonably good angular resolution and a high detection efficiency.

The design of DALI2 follows a similar concept to the original array DALI (Detector Array for Low Intensity radiation) [14, 15], which was developed for experiments at the old facility at RIKEN that provides light exotic beams with  $v/c \approx 0.3$ . DALI has been successfully employed, owing to its versatility with respect to detector configuration and its reasonably good angular and energy resolutions, in various in-beam  $\gamma$ -ray spectroscopy measurements [14, 16–30] (see Table 1). However, for higher-velocity beams, the performance of DALI is not optimized. DALI2 was designed to meet the criteria for the new RIBF facility, where the RI-beam velocity is typically 60% of the light speed, by improving the angular resolution and the detection efficiency. DALI2 was completed in 2002, and was used in a variety of experiments at the old RIKEN facility and more recently at the new facility. Gamma-transitions associated with direct reactions including Coulomb excitation, proton and alpha inelastic scattering, secondary fragmentation, and nucleon transfer reactions [31–55] have been studied (see

---

\*Corresponding author.

Email address: takesato@riken.jp (S. Takeuchi)

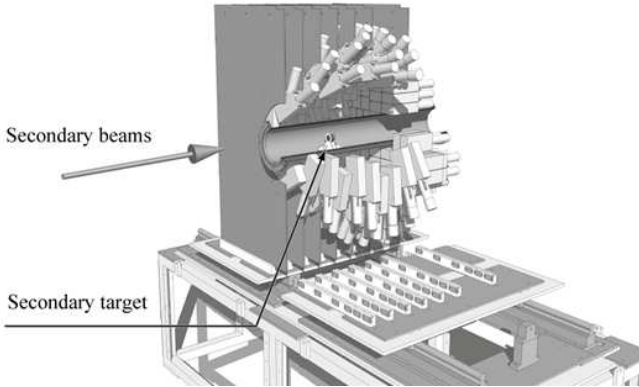


Figure 1: Schematic view of DALI2 in its standard configuration consisting of 186 NaI(Tl) crystals (see text for details).

Table 2). This article focuses on the design and performance of DALI2. Features of DALI2 in its early stage are briefly reported in ref. [56, 57].

## 2. Description of DALI2

### 2.1. Basic design

The center-of-mass energy resolution for  $\gamma$  rays emitted from moving sources depends on the uncertainty in the measurements of the angle of emission together with the velocity spread of the projectile and the intrinsic energy-resolution of the detector, which will be discussed in detail in Sect. 3. We adopted NaI(Tl) scintillator as the material for the detector crystal, since it offers a good compromise between intrinsic resolution, detection efficiency and costs. The angle measurement is made by employing a large number of (160 – 186 depending on the experimental condition) detectors at various distances from the target. The angle of  $\gamma$ -ray emission is also useful to characterize the  $\gamma$  transition, because the  $\gamma$ -ray angular distribution is sensitive to the transition multipolarity ( $\Delta L$ ), reflecting the nuclear spin-alignment produced during the reaction process that creates the nuclei being studied.

The array should cover a wide range of angles, to be sensitive to  $\Delta L$  and, more importantly, to reduce the uncertainty in extracting the total  $\gamma$  emission yield. Especially, small-angle measurements are important, because the  $\gamma$ -ray angular distribution is forward peaked in the laboratory frame due to the Lorentz boost. DALI2 can measure  $\gamma$  rays from  $15^\circ$  to enable to cover forward-peaked  $\gamma$ -ray angular distribution for  $\gamma$  emitters with the velocities around  $v/c = 0.6$  at the new RIBF facility.

### 2.2. Detector configuration and mechanical structure

Figure 1 shows an illustration of DALI2 in its standard configuration that can accommodate 186 NaI(Tl) detectors. Fast beams of unstable nuclei hit the target in a vacuum pipe, and DALI2 measures  $\gamma$  rays from ejectiles produced in excited

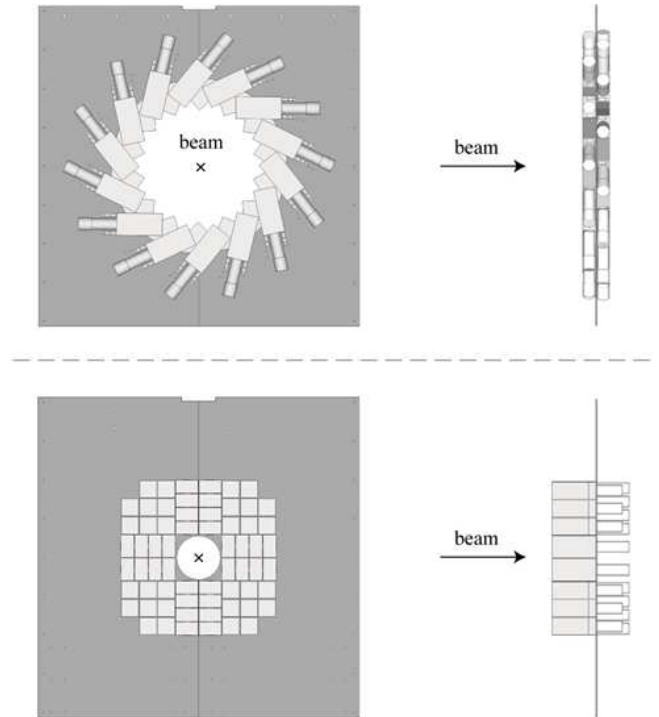


Figure 2: Top: layout of detectors in the 10<sup>th</sup> and 11<sup>th</sup> layers at 54 and 46 degrees, respectively. The other layers at backward angles are of similar configurations. Bottom: Detector configuration of the last layer for forward angle measurements.

states, for example, by inelastic scattering, in coincidence with the ejectiles that are identified by a device such as the ZeroDegree Spectrometer [59].

DALI2 is composed of three types of NaI(Tl) scintillator crystals. The first two types of crystals, which are manufactured by SAINT-GOBAIN [60] and SCIONIX [61], have dimensions of  $45 \times 80 \times 160 \text{ mm}^3$  and  $40 \times 80 \times 160 \text{ mm}^3$ , respectively. The third type of detector measures  $60 \times 60 \times 120 \text{ mm}^3$ , and was fabricated originally for DALI by BICRON [60]. The crystals of the former two types are coupled to 38-mm $\phi$  HAMAMATSU [62] R580 Photomultiplier tubes (PMTs), whereas the BICRON crystals use 50-mm $\phi$  HAMAMATSU R1306 PMTs. Each crystal is encapsulated in a 1-mm-thick aluminum housing. The typical energy resolution is about 9% (FWHM) for photons at 662 keV ( $^{137}\text{Cs}$  standard source).

As shown in Fig. 1, the detectors are arranged to form twelve layers set perpendicularly to the beam axis and a detector matrix covers the forward angles. Each layer consists of 6-14 detectors, which are mounted on a 5-mm-thick aluminum plate fixed to a support structure. For the 2<sup>nd</sup> to 11<sup>th</sup> layers, the two neighboring layers are attached to a single plate as shown in Fig. 2 (top). The last plate, for the most forward angles, fixes the forward-angle matrix consisting of 64 crystals as shown in Fig. 2 (bottom). The entire setup covers a range of polar angles in the laboratory frame between  $15^\circ$  and  $160^\circ$ . For the layers

Table 1: List of experiments performed with DALI.

Reaction	Beam	Energy (MeV/u)	Target	Thickness (mg/cm <sup>2</sup> )	Observables	Reference
Pb( <sup>32</sup> Mg, <sup>32</sup> Mg+ $\gamma$ )	<sup>32</sup> Mg	49.2	Pb	350	$B(E2)$ <sup>1</sup>	[14]
Pb( <sup>11</sup> Be, <sup>11</sup> Be+ $\gamma$ )	<sup>11</sup> Be	63.9	Pb	350	$d\sigma/d\Omega$ <sup>2</sup> , $B(E1)$	[16]
(CH <sub>2</sub> ) <sub>n</sub> ( <sup>10,12</sup> Be, <sup>10,12</sup> Be+ $\gamma$ )	<sup>10</sup> Be	59.2	(CH <sub>2</sub> ) <sub>n</sub>	90.2	$d\sigma/d\Omega$ , $\delta$ <sup>3</sup>	[17]
<sup>12</sup> C( <sup>10,12</sup> Be, <sup>10,12</sup> Be+ $\gamma$ )	<sup>12</sup> Be	53.8	C	89.8		
Pb( <sup>12</sup> Be, <sup>12</sup> Be+ $\gamma$ )	<sup>12</sup> Be	53.3	Pb	350.8	$E(1^-)$ <sup>4</sup> , $B(E1)$	[18]
<sup>12</sup> C( <sup>12</sup> Be, <sup>12</sup> Be+ $\gamma$ )		54.0	C	89.8		
<sup>9</sup> Be( <sup>36</sup> Si, <sup>34</sup> Mg+ $\gamma$ )	<sup>36</sup> Si	38.0	Be	385	$E(2_1^+)$ , $E(4_1^+)$ , $R(4^+/2^+)$ <sup>5</sup>	[19]
Pb( <sup>34</sup> Mg, <sup>34</sup> Mg+ $\gamma$ )	<sup>34</sup> Mg	44.9	Pb	693	$B(E2)$	[20]
<sup>2</sup> H( <sup>34</sup> Si, <sup>34</sup> Si+ $\gamma$ )	<sup>34</sup> Si	38.4	Liq.D <sub>2</sub> <sup>6</sup>	150	levels	[21]
<sup>12m</sup> Be $\rightarrow$ <sup>12</sup> Be*(2 <sup>+</sup> ) $\rightarrow$ <sup>12</sup> Be <sub>g.s.</sub>	<sup>12(m)</sup> Be	60.0	-	-	$E(0_2^+)$ , $\gamma$ - $\gamma$ angular correlation	[22]
<sup>1</sup> H( <sup>30</sup> Ne, <sup>30</sup> Ne+ $\gamma$ )	<sup>30</sup> Ne	48.0	Liq.H <sub>2</sub>	186	$E(2_1^+)$ , $B(E2)$	[23]
Pb( <sup>15</sup> O, <sup>15</sup> O+ $\gamma$ )	<sup>15</sup> O	85.0	Pb	1480	$\Gamma_\gamma$ of the 3/2 <sup>+</sup> state at 6.793 MeV	[24]
Pb( <sup>16</sup> C, <sup>16</sup> C+ $\gamma$ )	<sup>16</sup> C	52.7	Pb	50	$d\sigma/d\Omega$ , $B(E2)$	[25]
<sup>9</sup> Be( <sup>16</sup> C, <sup>16</sup> C+ $\gamma$ )	<sup>16</sup> C	34.6	Be	370	lifetime, $B(E2)$	[26]
<sup>12</sup> C( <sup>15,17</sup> B, <sup>15,17</sup> B+ $\gamma$ )	<sup>15,17</sup> B	72.0	C	377	levels, $d\sigma/d\Omega$ , $\delta$	[27]
Pb( <sup>28</sup> Ne, <sup>28</sup> Ne+ $\gamma$ )	<sup>28</sup> Ne	46.0	Pb	693	$B(E2)$	[28]
<sup>12</sup> C( <sup>28</sup> Ne, <sup>28</sup> Ne+ $\gamma$ )			C	339		
Pb( <sup>20</sup> Mg, <sup>20</sup> Mg+ $\gamma$ )	<sup>20</sup> Mg	58.0	Pb	226	$d\sigma/d\Omega$ , $B(E2)$	[29]
<sup>12</sup> C( <sup>20</sup> Mg, <sup>20</sup> Mg+ $\gamma$ )			C	118		
<sup>1</sup> H( <sup>18</sup> C, <sup>17</sup> C+ $\gamma$ )	<sup>18</sup> C	81.0	Liq.H <sub>2</sub>	120	levels, $\sigma$ <sup>7</sup> , $d\sigma/dP_x$ <sup>8</sup>	[30]
<sup>1</sup> H( <sup>19</sup> C, <sup>18</sup> C+ $\gamma$ )	<sup>19</sup> C	68.0				

1  $B(EL/ML)$ : transition probability for EL or ML transition

2  $d\sigma/d\Omega$ : differential cross section

3  $\delta$ : deformation length

4  $E(J^\pi)$ : energy of excited state

5  $R(4^+/2^+)$ : energy ratio between the 4<sup>+</sup> and 2<sup>+</sup> states

6 Liq.D<sub>2</sub>, Liq.H<sub>2</sub>: liquid targets of deuterium and hydrogen provided by CRYogenic ProTon and Alpha target system (CRYPTA) [58]

7  $\sigma$ : total or angle integrated cross section

8  $d\sigma/dP_x$ : parallel momentum distribution

Table 2: List of experiments performed with DALI2.

Reaction	Beam	Energy (MeV/u)	Target	Thickness (mg/cm <sup>2</sup> )	Observables	Reference
$^1\text{H}(^{27}\text{F}, ^{25,26,27}\text{F}+\gamma)$	$^{27}\text{F}$	39.6	Liq.H <sub>2</sub>	210	levels, $\sigma$	[31]
$^1\text{H}(^{17}\text{B}, ^{12,14,15,17}\text{B}+\gamma)$	$^{17}\text{B}$	43.0	Liq.H <sub>2</sub>	180	levels, $\sigma$	[32]
$^1\text{H}(^{19}\text{C}, ^{17,19}\text{C}+\gamma)$	$^{19}\text{C}$	49.4	Liq.H <sub>2</sub>	190	levels, $\sigma, \beta^9$	[33]
$^1\text{H}(^{17}\text{C}, ^{17}\text{C}+\gamma)$	$^{17}\text{C}$	43.3				
$^1\text{H}(^{17}\text{B}, ^{17}\text{B}+\gamma)$	$^{17}\text{B}$	43.8	Liq.H <sub>2</sub>	190	$d\sigma/d\Omega, \delta$	[34]
$^1\text{H}(^{16}\text{C}, ^{16}\text{C}+\gamma)$	$^{16}\text{C}$	33.0	Liq.H <sub>2</sub>	225	$d\sigma/d\Omega, \delta$	[35]
$^4\text{He}(^{22}\text{O}, ^{23}\text{F}+\gamma)$	$^{22}\text{O}$	35.0	Liq.He	100	levels, $d\sigma/d\Omega$	[36]
$^4\text{He}(^{23}\text{F}, ^{23}\text{F}+\gamma)$	$^{23}\text{F}$	41.5				
$^4\text{He}(^{24}\text{F}, ^{23}\text{F}+\gamma)$	$^{24}\text{F}$	36.0				
$^4\text{He}(^{25}\text{Ne}, ^{23}\text{F}+\gamma)$	$^{25}\text{Ne}$	42.7				
$\text{CD}_2(^{22}\text{O}, ^{22}\text{O}+\gamma)$	$^{22}\text{O}$	34.0	CD <sub>2</sub>	30	$\sigma, \beta$	[37]
$^1\text{H}(^{30}\text{Na}, ^{30}\text{Na}+\gamma)$	$^{30}\text{Na}$	50.0	Liq.H <sub>2</sub>	210	levels, $\sigma, \beta$	[38]
$^1\text{H}(^{31}\text{Na}, ^{30,31}\text{Na}+\gamma)$	$^{31}\text{Na}$					
$^1\text{H}(^{33}\text{Mg}, ^{33}\text{Mg}+\gamma)$	$^{33}\text{Mg}$					
$^1\text{H}(^{34}\text{Mg}, ^{33,34}\text{Mg}+\gamma)$	$^{34}\text{Mg}$					
$^1\text{H}(^{28}\text{Ne}, ^{27,28}\text{Ne}+\gamma)$	$^{28}\text{Ne}$	51.3	Liq.H <sub>2</sub>	210	levels, $\sigma$	[39]
$\text{Pb}(^{26}\text{Ne}, ^{26}\text{Ne}+\gamma)$	$^{26}\text{Ne}$	54.0	Pb	230	levels, $d\sigma/d\Omega, B(E2)$	[40]
$^9\text{Be}(^{18}\text{C}, ^{17}\text{C}+\gamma)$	$^{18}\text{C}$	79.0	Be	370	lifetime, $B(M1)$	[41]
$^9\text{Be}(^{18}\text{C}, ^{18}\text{C}+\gamma)$	$^{18}\text{C}$	79.0	Be	370	lifetime, $B(E2)$	[42]
$^9\text{Be}(^{16}\text{C}, ^{16}\text{C}+\gamma)$	$^{16}\text{C}$	72.0				
$\text{Pb}(^{76,80}\text{Ge}, ^{76,80}\text{Ge}+\gamma)$	$^{76,80}\text{Ge}$	37.0	Pb	175	levels, $B(E2; 2_2^+ \rightarrow 0_{g.s.}^+)$	[43]
$\text{Pb}(^{20}\text{C}, ^{20}\text{C}+\gamma)$	$^{20}\text{C}$	37.6	Pb	1445	$\sigma, B(E2)$	[44]
$^1\text{H}(^{20}\text{C}, ^{20}\text{C}+\gamma)$		41.4	Liq.H <sub>2</sub>	190		
$^1\text{H}(^{60}\text{Cr}, ^{60}\text{Cr}+\gamma)$	$^{60}\text{Cr}$	42.0	Liq.H <sub>2</sub>	72	$E(4_1^+), R(4^+/2^+), \sigma, \delta$	[45]
$^1\text{H}(^{62}\text{Cr}, ^{62}\text{Cr}+\gamma)$	$^{62}\text{Cr}$	39.0				
$^1\text{H}(^{32}\text{Mg}, ^{32}\text{Mg}+\gamma)$	$^{32}\text{Mg}$	46.5	Liq.H <sub>2</sub>	157	$E(4_1^+), R(4^+/2^+),$ levels, $d\sigma/d\Omega, \delta$	[46]
$\text{C}(^{32}\text{Ne}, ^{32}\text{Ne}+\gamma)$	$^{32}\text{Ne}$	226.0	C	2540	$E(2_1^+)$	[47]
$\text{C}(^{33}\text{Na}, ^{32}\text{Ne}+\gamma)$	$^{33}\text{Na}$	245.0				
$\text{C}(^{32}\text{Na}, ^{31,32}\text{Na}+\gamma)$	$^{32}\text{Na}$	230	C	2540	levels	[48]
$\text{C}(^{33}\text{Na}, ^{33}\text{Na}+\gamma)$	$^{33}\text{Na}$	-				
$\text{C}(^{34}\text{Na}, ^{33}\text{Na}+\gamma)$	$^{34}\text{Na}$	250				
$\text{Pb}(^{21}\text{N}, ^{21}\text{N}+\gamma)$	$^{21}\text{N}$	52.0	Pb	1445	$\sigma, B(E2)$	[49]
$^1\text{H}(^{21}\text{N}, ^{19,21}\text{N}+\gamma)$		48.1	Liq.H <sub>2</sub>	190		
$\text{Pb}(^{28}\text{S}, ^{28}\text{S}+\gamma)$	$^{28}\text{S}$	53.0	Pb	348	$d\sigma/d\Omega, B(E2)$	[50]
$(\text{CH}_2)_n(^{32}\text{Mg}, ^{32}\text{Mg}+\gamma)$	$^{32}\text{Mg}$	190.0	$(\text{CH}_2)_n$	2130	$d\sigma/d\Omega, \beta$	[51]
$\text{C}(^{32}\text{Mg}, ^{32}\text{Mg}+\gamma)$			C	2540		
$\text{C}(^{44}\text{S}, ^{40,42}\text{Si}+\gamma)$	$^{44}\text{S}$	210.0	C	2540	$E(4_1^+), R(4^+/2^+), \sigma$	[52]
$\text{C}(^{40}\text{S}, ^{38}\text{Si}+\gamma)$	$^{40}\text{S}$					
$^1\text{H}(^{58}\text{Ti}, ^{58}\text{Ti}+\gamma)$	$^{58}\text{Ti}$	42.0	Liq.H <sub>2</sub>	72	$E(2_1^+),$ levels, $\sigma, \delta$	[53]
$^9\text{Be}(^{55}\text{Sc}, ^{54}\text{Ca}+\gamma)$	$^{55}\text{Sc}$	220	Be	1848	$E(2_1^+),$ levels	[54]
$^9\text{Be}(^{56}\text{Ti}, ^{54}\text{Ca}+\gamma)$	$^{56}\text{Ti}$	230				
$\text{C}(^{40}\text{Si}, ^{38}\text{Mg}+\gamma)$	$^{40}\text{Si}$	226	C	2540	$E(4_1^+), R(4^+/2^+)$	[55]
$\text{C}(^{39}\text{Al}, ^{38}\text{Mg}+\gamma)$	$^{39}\text{Al}$	219				
$\text{C}(^{37}\text{Al}, ^{34,36}\text{Mg}+\gamma)$	$^{37}\text{Al}$	247				
$\text{C}(^{36}\text{Mg}, ^{34}\text{Mg}+\gamma)$	$^{36}\text{Mg}$	236				

9  $\beta$ : deformation parameter

near  $90^\circ$ , the distance between the target and the center of each detector is about 30 cm, which is shortest among the detectors in different layers. In this standard DALI2 configuration, the opening angle spanned by a NaI(Tl) crystal is approximately  $6^\circ$  (FWHM) for detectors at  $60^\circ$  to the beam line, where the Doppler-shift effect is largest for ejectiles with  $v/c = 0.6$ .

For maintenance purposes, each layer is subdivided into two parts, and each part can be moved from its regular position. The geometrical configuration of the crystals (or detectors) can be easily changed according to experimental requirements either by relocating detectors on the plates or by changing the layout of the plates. This flexibility also enables different types of experiments, to be performed, such as life-time measurements using the recoil shadow method [42].

### 2.3. Electronics

A typical diagram for signal handling for DALI2 is shown in Fig. 3. A multichannel power supply system (CAEN [63] SY1527) provides a high voltage of around 1200 V to each PMT. The signals from each PMT are fed into a shaping amplifier (CAEN N568B) and split into two separate signals for energy and timing measurements. The signals for the energy measurements, outputs of N568B shaped with  $3\text{-}\mu\text{s}$  time constant, are delivered to a peak-sensing analog-to-digital converter (CAEN V785 ADC). Fast-out signals differentially shaped with 100-ns time constant are fed into a time-to-digital converter (CAEN V1190A TDC) through a constant-fraction discriminator (CAEN V812 CFD). To trigger the data acquisition, a logic signal ( $\gamma$  trigger) is generated by taking the ‘‘OR’’ logic of the CFD outputs. This signal is also used as a gate signal for the ADC with  $4\ \mu\text{s}$  width and a trigger signal for the TDC. The V1190A TDC module has an adjustable time window with a time offset relative to the trigger signal, which are programmable via a VME control bus. In most of the experiments, the width of time window and the offset are set to  $2\ \mu\text{s}$  and  $-1\ \mu\text{s}$ , which enable to measure the  $\gamma$ -ray timing relative to the trigger signal, arrived about  $1\ \mu\text{s}$  later. Thus, additional delays are not necessary for signals from CFDs. Data acquisition is performed by the system developed for experiments at RIBF [64]. For in-beam  $\gamma$ -ray spectroscopy experiments, the entire acquisition system is triggered by a coincidence signal generated by the ‘‘AND’’ logic of the  $\gamma$ -ray and beam triggers. A typical trigger rate is around 1 kHz and the dead time of the data acquisition is lower than  $100\ \mu\text{s}$ .

## 3. Performance

### 3.1. Measurements of $\gamma$ transitions and energy resolution

As mentioned earlier, the resolution for the  $\gamma$ -transition energy is affected by the Doppler effect in addition to the intrinsic resolution of the detector. Experimental conditions such as target thicknesses, beam velocities, or beam directions also influence the energy resolution as described below. The energy in the laboratory frame of reference,  $E_{\text{lab}}$ , of  $\gamma$  rays emitted from fast-moving nuclei is shifted from the  $\gamma$ -ray energy in the

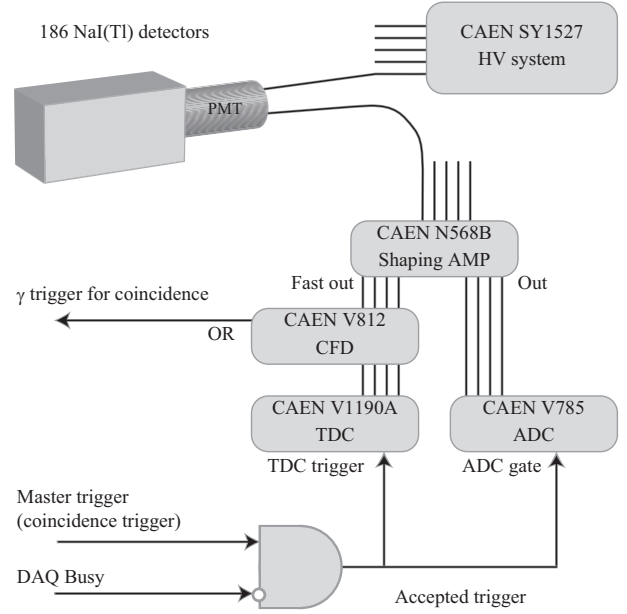


Figure 3: Schematic diagram of signal handling for DALI2.

center-of-mass (CM) frame,  $E_{\text{CM}}$ , i.e., the transition energy in the nucleus of interest. These energies are related as,

$$E_{\text{CM}} = \gamma(1 - \beta \cos \theta_{\text{lab}})E_{\text{lab}}, \quad (1)$$

where  $\theta_{\text{lab}}$ ,  $\beta$  and  $\gamma$  denote respectively the  $\gamma$ -ray emission angle with respect to the direction of the moving nucleus, the velocity relative to the light speed ( $v/c$ ) of the moving nucleus and the Lorentz factor. Accordingly, the  $E_{\text{CM}}$  resolution depends on the uncertainties in the  $\gamma$ -ray angle,  $\Delta\theta$ , the beam velocity,  $\Delta\beta$ , and the measured  $\gamma$  energy,  $\Delta E_{\text{lab}}$ , according to

$$\begin{aligned} \left(\frac{\Delta E_{\text{CM}}}{E_{\text{CM}}}\right)^2 &= \left(\frac{\beta \sin \theta_{\text{lab}}}{1 - \beta \cos \theta_{\text{lab}}}\right)^2 (\Delta\theta_{\text{lab}})^2 \\ &+ \left(\frac{\beta\gamma^2(\beta - \cos \theta_{\text{lab}})}{1 - \beta \cos \theta_{\text{lab}}}\right)^2 \left(\frac{\Delta\beta}{\beta}\right)^2 \\ &+ \left(\frac{\Delta E_{\text{lab}}}{E_{\text{lab}}}\right)^2. \end{aligned} \quad (2)$$

The angular resolution  $\Delta\theta_{\text{lab}}$  depends on the detector size and its distance from the  $\gamma$ -ray emission source. The uncertainty of the beam velocity  $\Delta\beta$  is determined by the beam-energy spread and the thickness of the reaction target where the beam loses its energy. Figure 4 indicates the energy resolution for a 1-MeV  $\gamma$  ray emitted from a nucleus with  $\beta = 0.6$  as a function of  $\theta_{\text{lab}}$ . Individual contributions from the three terms in Eq. 2 are shown separately. An intrinsic detector resolution  $\Delta E_{\text{lab}}/E_{\text{lab}}$  of 7% (FWHM), an averaged angular resolution ( $\Delta\theta_{\text{lab}}$ ) of 7 degrees (FWHM), and a velocity spread  $\Delta\beta/\beta = 10\%$  are assumed, which are typical values for experiments at the new RIBF facility. As seen in the figure, DALI2 is designed so that the overall contributions from the angular- and velocity-resolutions are similar to the NaI(Tl) intrinsic resolution, and hence a modest angular dependence of the  $E_{\text{CM}}$  resolution is achieved.

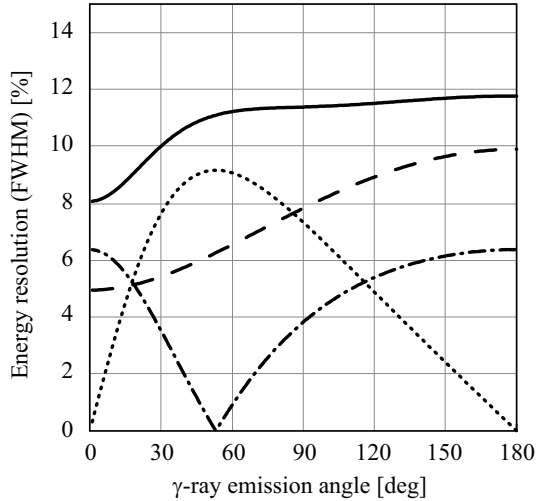


Figure 4: Expected energy resolution for 1-MeV photons in the center-of-mass system plotted as a function of  $\gamma$ -ray emission angle  $\theta_{lab}$  (solid curve). The contributions from the intrinsic energy resolution (dashed curve), the finite opening angle of the detector (dotted curve), and the velocity spread of  $\gamma$  emitters (dash-dotted curve) are also shown. See details in the text.

Figure 5 shows  $\gamma$ -ray energy spectra measured by DALI2 for the two-proton removal reaction feeding states in  $^{42}\text{Si}$  by radioactive  $^{44}\text{S}$  beams with  $\beta = 0.6$  and a carbon target ( $2.54 \text{ g/cm}^2$ ) [52]. The spectrum in the laboratory frame, Fig. 5(a), does not exhibit any distinct peaks except for the one at 511 keV due to  $e^+e^-$  annihilation. The rise at low energies is caused by sources of atomic background [65–67]. On the other hand, a few peaks are seen in the spectrum in the CM frame of  $^{42}\text{Si}$  Fig. 5(b), obtained by correcting the Doppler shift using measured  $\gamma$  emission angles. The most prominent peak at 742 keV corresponds to the transition from the first excited  $2^+$  state to the  $0^+$  ground state in  $^{42}\text{Si}$ . Its width (91 keV at FWHM) is consistent with the above estimate and agrees well with Monte-Carlo simulations, which will be described in the following section. Other weaker peaks also correspond to transitions in  $^{42}\text{Si}$ . This is confirmed, for example, for the 1431-keV peak, which is more pronounced in the  $\gamma$ - $\gamma$  coincidence spectrum gated by the 742-keV  $\gamma$  rays shown in the inset of Fig. 5(b). As demonstrated in this example, DALI2 is capable of performing in-beam  $\gamma$ -ray spectroscopy experiments with secondary beams at very high velocities of  $\beta \sim 0.6$ .

### 3.2. Detection efficiency

Table 3 shows full-energy-peak efficiencies for  $\beta$  values of 0.0, 0.3 and 0.6, at CM photon energies of 500 keV, 1 MeV and 2 MeV, obtained from Monte Carlo simulations using the code GEANT3 [68] with the standard configuration of DALI2 described in Sec. 2.2 and an isotropic distribution of  $\gamma$  rays. Effects of  $\gamma$ -ray absorption in material surrounding the target, the target holder (or the target cell in case of liquid target [58]) and the wall of the target chamber, for example, should be increased for more realistic measurements (they are not accounted for in the results listed in Table 3). These effects reduce the efficiency typically by 20% of the values listed in Table 3.

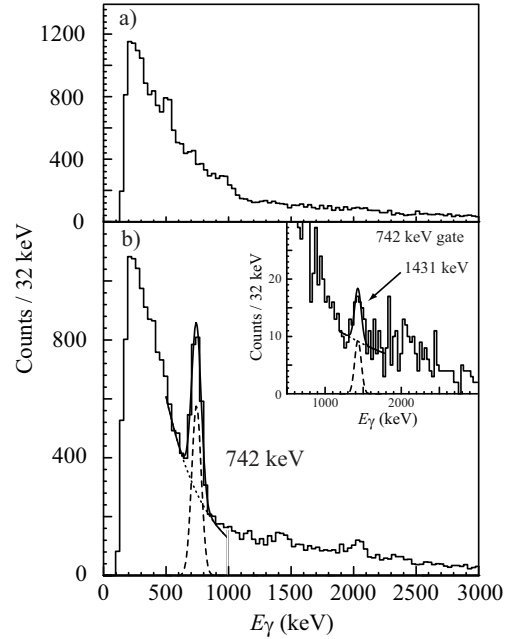


Figure 5:  $\gamma$ -ray energy spectra obtained for  $^{42}\text{Si}$  in the two-proton removal reaction experiments with fast RI beams of  $^{44}\text{S}$  [52] without the correction for Doppler-shift effects (a) and with the correction (b). The inset of b) shows a  $\gamma$ - $\gamma$  coincidence spectrum gated on the 742-keV  $\gamma$ -ray line. The solid curves in b) represent the result of fits by using Gaussian function (dashed curves) and exponential background (dotted curves).

Figure 6 shows the angular distribution for different  $\beta$  and  $\Delta L$  values, where the spin of the nucleus is assumed to be fully aligned in the plane perpendicular to the beam axis by the reaction (in the case of  $\Delta L = 1$  and  $\Delta L = 2$ ). DALI2 has an angular coverage of  $\sim 15^\circ$  to  $\sim 160^\circ$  with respect to the beam axis, resulting in a solid-angle coverage of more than 90%. Therefore, the uncertainty in the total  $\gamma$  yield due to the incomplete angle-coverage is small. For example, the different assumptions for the multipolarities ( $\Delta L = 0, 1, 2$ ) and the velocities ( $\beta = 0.0, 0.3, 0.6$ ) shown in Fig. 6 indicate a change of 6% at most relative to the total yield. The uncertainty might be even lower, since the alignment is lower in most cases.

The Monte Carlo simulation was tested using measurements with standard stationary  $\gamma$  sources,  $^{22}\text{Na}$ ,  $^{60}\text{Co}$  and  $^{137}\text{Cs}$ , placed at the center of DALI2. In Fig. 7, the results of a GEANT3 simulation (solid curve) and measured efficiencies (open circles) are compared. They are consistent within 5%, indicating a satisfactory accuracy of the simulation. The inset of Fig. 7 shows a  $\gamma$  spectrum taken with a  $^{137}\text{Cs}$  source using all the detectors of DALI2. The dashed curve represents the simulated detector response to 662-keV photons. As shown in the figure, the experimental spectrum is reproduced well by the simulated response with an energy resolution of 9% (mentioned in Sect. 2.2) and a component of measured background (dotted curve).

### 3.3. Add-back analysis

A higher detection efficiency can be achieved by changing the detector configuration so that the average distance between

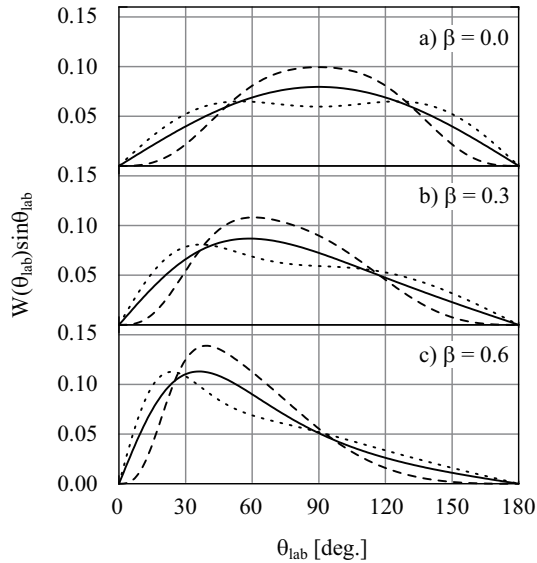


Figure 6: Angular distributions in the laboratory-frame for 1-MeV photons emitted from sources moving with velocities of a)  $\beta = 0.0$ , b)  $\beta = 0.3$ , and c)  $\beta = 0.6$ . The respective solid, dashed, and dotted curves show the distributions for isotropic  $\gamma$  emission in the center-of-mass system, transitions with multipolarities of  $\Delta L = 1$  and  $\Delta L = 2$ . Note that full spin-alignment is assumed for the cases of  $\Delta L = 1$  and  $\Delta L = 2$ .

the target and each detector is shorter than the standard setup described in Sect. 2.2. However, this solution has a drawback: The  $E_{CM}$  resolution becomes worse because a larger opening angle is subtended by each detector, resulting in a more pronounced Doppler broadening effect. An alternative way is to employ the so-called add-back analysis without changing the configuration.

In the add-back analysis, signals from a group of two or more neighboring detectors (a “cluster”) were assumed to be generated from a Compton-scattered event. The sum of the energies measured in a given cluster is used to generate a  $\gamma$ -ray energy spectrum. The detector with the largest energy deposit in the cluster is assumed to be the one where the first interaction takes place, and its position is used for the Doppler-shift correction. By this add-back analysis, the photo-peak efficiency increases by 30% for 1-MeV  $\gamma$ -rays emitted from nuclei moving at the velocity of  $\beta = 0.5$ . The possibility of misassignment of the first interaction point is found to be below 20% of the cluster events using Monte Carlo simulations (under the same condition as above). These events are taken into account as a part of the response function used for the fit. In the proton inelastic scattering experiment to study  $^{32}\text{Mg}$  [46], the efficiency for 1-

Table 3: Simulated efficiencies of DALI2.

$E_\gamma$ (MeV)	$\beta = 0.0$	$\beta = 0.3$	$\beta = 0.6$
0.5	43%	40%	35%
1.0	24%	24%	20%
2.0	14%	13%	10%

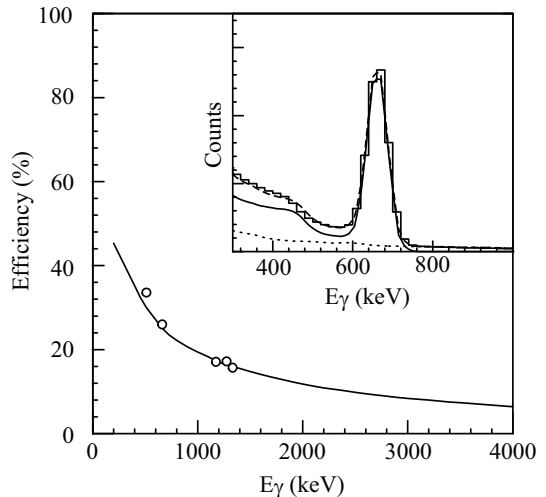


Figure 7: Full-energy-photopeak efficiencies measured with the standard sources  $^{137}\text{Cs}$ ,  $^{60}\text{Co}$  and  $^{22}\text{Na}$  (open circles) and the one obtained by a simulation (solid curve). The inset shows an energy spectrum for the  $^{137}\text{Cs}$  source using all the detectors of DALI2.

MeV  $\gamma$  rays from moving nuclei with  $v/c \sim 0.3$  was increased by about 20% when the add-back analysis was adopted. In addition to increasing the detection efficiency, the add-back analysis improves the peak-to-background ratio, particularly for high-energy photons by reducing the Compton tails. In order to obtain the location of a full-energy-peak in a  $\gamma$  spectrum, the non-linear response of the NaI(Tl) light output should be taken into account in the add-back analysis. The non-linearity is known to be sizable below 400 keV [69, 70], and the resultant shift by this effect was estimated to be 5 keV in the analysis of the proton inelastic scattering on  $^{32}\text{Mg}$  [46].

### 3.4. $\gamma$ - $\gamma$ coincidences

The high efficiency of DALI2 enables  $\gamma$ - $\gamma$  coincidence measurements with reasonable statistics. Reduction of the statistics compared with the case of the singles spectrum is by typically a factor of five for 1-MeV photons (see Table 3). It enables coincidence measurements to establish  $\gamma$ -ray cascades and hence level schemes of unstable nuclei produced with small yields. In the case of the two-proton removal reaction on  $^{44}\text{S}$  to  $^{42}\text{Si}$  [52] described in Sect. 3.1, the peak at 1431 keV becomes more pronounced in the coincidence spectrum gated on the 742-keV line relative to the singles spectrum, as shown in Fig. 5(b) and its inset. This coincidence relationship for the  $2^+$  and  $4^+$  states in  $^{42}\text{Si}$  was supported by taking into account systematic trends for the states populated by the two nucleon removal reaction. This method has been applied successfully to establish low-lying level schemes, typically composed of  $2^+$  and  $4^+$  states, for many neutron-rich isotopes at RIBF, demonstrating the capability of the DALI2 array in in-beam  $\gamma$ -ray spectroscopy experiments for nuclei far from stability.

### 3.5. Angular distributions

As demonstrated in Fig. 6,  $\gamma$  rays from aligned nuclei have angular distributions that depend on transition multipolarities.

Since a relatively large alignment is expected for the products of direct reactions at the RIBF energies, and therefore sizable sensitivity to the multipolarity is expected, the angular distribution measurements by DALI2 should provide information on the spins and parities of unknown excited states. Figure 8 shows an example. The angular distribution is for  $\gamma$  rays from the first  $2^+$  excited state at  $E_x = 885$  keV in  $^{32}\text{Mg}$  populated by inelastic proton scattering [46]. The solid curve indicates the distribution, where the spin alignment was obtained from distorted-wave calculations assuming  $\Delta L = 2$  with the code ECIS97 [71]. The theoretical angular distribution agrees well with the data taken by DALI2, indicating the usefulness of angular-distribution measurements in determining  $\gamma$ -ray multipolarities. The large angular coverage of DALI2 is ideal for this purpose.

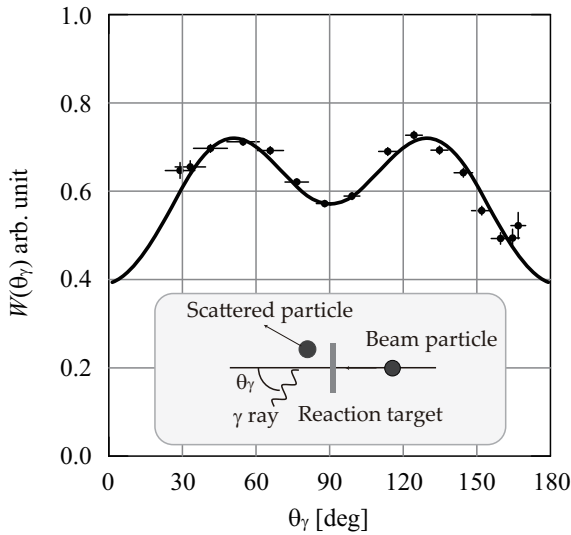


Figure 8: Angular distribution of 885 keV  $\gamma$  rays emitted from moving  $^{32}\text{Mg}$  nuclei inelastically excited to the  $2^+$  state with a hydrogen target [46]. The distribution is plotted in the rest frame of  $^{32}\text{Mg}$ . The solid curve shows the result of a distorted-wave calculation for proton inelastic scattering assuming the multipolarity  $\Delta L = 2$ .

Table 4: Basic parameters of DALI and DALI2. The efficiencies and energy resolutions are for 1-MeV  $\gamma$  rays.

$\beta = v/c$	DALI		DALI2		
	0.0	0.3	0.0	0.3	0.6
number of detectors	~60		160	186	
number of layers	6~8		16		
angle coverage (degree)	~50° – ~150°		~15° – ~160°		
average $\Delta\theta$ (FWHM)	10°		7°		
$\Delta E/E$ (FWHM)	10%	12%	7%	8%	10%
Efficiency	13%	10%	24%	24%	20%

## 4. Discussion

Table 4 summarizes the efficiencies and resolutions of DALI and DALI2 for 1-MeV  $\gamma$  rays emitted from  $\gamma$ -ray sources with different velocities. As mentioned in Sect. 1, DALI2 was designed to accommodate higher beam velocities at the new RIBF facility. As indicated in the table, the performance of 20% efficiency and 10% resolution at FWHM for DALI2 at  $\beta = 0.6$ , the typical velocity of RI beams in the new RIBF facility, is preserved or even improved on compared to DALI at  $\beta = 0.3$ , the velocity at RIPS in the old facility. This resolution is satisfactory for spectroscopy of low-lying states in even-even exotic nuclei in light- and medium-mass regions, where their level spacings are typically larger than 500 keV. The high efficiency, in the ~20% range, enables  $\gamma$ - $\gamma$  coincidence measurements even for beam intensities as low as 1 Hz, making spectroscopic studies of nuclei very far from stability feasible.

However, in order to extend our research opportunities to heavier exotic nuclei, such as the ones involved in the r-process nucleosynthesis, and to odd nuclei with narrower level spacings, a higher resolution device is needed. An array called SHOGUN (Scintillator based High-resolution Gamma-ray spectrometer for Unstable Nuclei) [72, 73] with  $\text{LaBr}_3(\text{Ce})$  crystals was proposed for that purpose. The high intrinsic resolution of  $\text{LaBr}_3(\text{Ce})$  ( $\approx 2\%$  (FWHM) at 1.3 MeV is expected for a small-size crystal) is ideal for a higher energy-resolution array for fast-moving  $\gamma$  emitters. The high  $\gamma$ -ray absorption coefficient of  $\text{LaBr}_3(\text{Ce})$  material is another advantage for RI-beam induced experiments at RIBF. A design with one thousand crystals enables almost constant spread of Doppler shift for all the detectors by setting different distance from the target depending on the angle relative to the beam direction. The average opening angle of each detector is  $\sim 3^\circ$ . The expected energy resolution and efficiency for a  $4\pi$  geometry are 3.6% (FWHM) and 40%, respectively, for 1-MeV  $\gamma$  rays emitted from nuclei moving at 200 MeV/u [72]. For more realistic estimate, the effect of velocity difference in the target discussed in Sect. 3.1 should be taken into account. For example, with a target causing beam-velocity change of 5% (10%), the overall energy resolution becomes 4.6% (7.2%).

Ge-based  $\gamma$ -ray trackers like GRETA [6, 7] and AGATA [9] can improve the energy resolution. Their expected high angular resolution together with the high intrinsic resolution of Ge detectors can be exploited for applications to precision spectroscopy with a thin target. As already discussed, the target thickness, relevant to the velocity spread  $\Delta\beta/\beta$ , affects the energy resolution after correction of the Doppler-shift effect. In the condition with the target thickness causing 5% change of the velocity of  $\beta = 0.5$ , similar to the case discussed for SHOGUN, the expected energy resolution for 1-MeV  $\gamma$  ray is to be 4.7% for the AGATA array [74], which is not different from the number for SHOGUN. To achieve higher resolution, the velocity should be better controlled. For example, the velocity should be determined in 0.3% precision with  $\beta = 0.5$  to obtain energy-resolution values 10% larger than the limiting value caused by other conditions as the intrinsic resolution [74]. The simplest solution is to use a very thin target, requiring high-intensity



beams to keep the beam-target luminosity.

Ge-based  $\gamma$ -ray trackers are useful in spectroscopy experiments with fast beams of unstable nuclei not very far from the stability line, where the RI-beam intensity is expected to be high. On the other hand, in experiments for nuclei very far from stability line served as beams of a typical intensity of 1 Hz, use of scintillator-based arrays such as DALI2 or SHOGUN is a solution with good cost effectiveness.

## 5. Summary

We have developed a NaI(Tl) detector array, DALI2, for in-beam  $\gamma$ -ray spectroscopy experiments at RIKEN RIBF. The array consists of 186 NaI(Tl) detectors in its standard configuration. It subtends a large solid angle with a high efficiency. A typical full-energy-photopeak resolution of 10% (FWHM) and 20% efficiency for photons with 1 MeV in the rest frame of the  $\gamma$ -ray emitter with  $\beta \sim 0.6$  can be achieved. The DALI2 array has been applied to various in-beam  $\gamma$ -ray spectroscopy experiments at RIBF successfully, and will be used in many more experiments to study structures of light and medium-mass exotic nuclei mostly with even numbers of protons and neutrons. The ZeroDegree [59], SAMURAI [75], or SHARAQ [76] spectrometers will be used to detect the reaction residues. For studies of heavy or odd-mass nuclei, the SHOGUN array, with superior energy resolution, is planned.

## Acknowledgments

The construction of DALI2 was supported financially by Research Center for Measurement in Advanced Science (RC-MAS) of Rikkyo University and RIKEN Nishina Center for Accelerator-Based Science. We thank the RCMAS staff members and collaborators of experiments that were performed with DALI and DALI2. We are grateful to Dr. D. Steppenbeck for proofreading of this article.

## References

- [1] V. Metag, et al., Nucl. Phys. A 409 (1983) 331c.
- [2] I.-Y. Lee, Nucl. Phys. A 520 (1990) 641c.
- [3] F. A. Beck, Prog. Part. Nucl. Phys 28 (1992) 443.
- [4] J. Simpson, APH N.S., Heavy Ion Physics 11 (2000) 159.
- [5] W. F. Mueller, et al., Nucl. Instrum. Methods Phys. Res., Sect. A 466 (2001) 492.
- [6] I. Y. Lee, et al., Rep. Prog. Phys. 66 (2003) 1095.
- [7] I. Lee, et al., Nucl. Phys. A 746 (2004) 255c.
- [8] S. Shimoura, et al., Nucl. Instrum. Methods Phys. Res., Sect. A 525 (2004) 188.
- [9] S. Akkoyun, et al., Nucl. Instrum. Methods Phys. Res., Sect. A 668 (2012) 26.
- [10] K. Wisshak, et al., Nucl. Instrum. Methods Phys. Res., Sect. A 292 (1990) 595.
- [11] D. Weisshaar, et al., Nucl. Instrum. Methods Phys. Res., Sect. A 624 (2010) 615.
- [12] N. Warr, et al., Eur. Phys. J. A 49 (2013) 40.
- [13] SPECIAL ISSUE: RESEARCH IN RI BEAM FACTORY, Prog. Theor. Exp. Phys. (2012).
- [14] T. Motobayashi, et al., Phys. Lett. B 346 (1995) 9.
- [15] T. Nishio, et al., RIKEN Accel. Prog. Rep. 29 (1996) 184.
- [16] T. Nakamura, et al., Phys. Lett. B 394 (1997) 11.
- [17] H. Iwasaki, et al., Phys. Lett. B 481 (2000) 7.
- [18] H. Iwasaki, et al., Phys. Lett. B 491 (2000) 8.
- [19] K. Yoneda, et al., Phys. Lett. B 499 (2001) 233.
- [20] H. Iwasaki, et al., Phys. Lett. B 522 (2001) 227.
- [21] N. Iwasa, et al., Phys. Rev. C 67 (2003) 064315.
- [22] S. Shimoura, et al., Phys. Lett. B 560 (2003) 31.
- [23] Y. Yanagisawa, et al., Phys. Lett. B 566 (2003) 84.
- [24] K. Yamada, et al., Phys. Lett. B 579 (2004) 265.
- [25] Z. Elekes, et al., Phys. Lett. B 586 (2004) 34.
- [26] N. Imai, et al., Phys. Rev. Lett. 92 (2004) 062501.
- [27] Y. Kondo, et al., Phys. Rev. C 71 (2005) 044611.
- [28] H. Iwasaki, et al., Phys. Lett. B 620 (2005) 118.
- [29] N. Iwasa, et al., Phys. Rev. C 78 (2008) 024306.
- [30] Y. Kondo, et al., Phys. Rev. C 79 (2009) 014602.
- [31] Z. Elekes, et al., Phys. Lett. B 599 (2004) 17.
- [32] R. Kanungo, et al., Phys. Lett. B 608 (2005) 206.
- [33] Z. Elekes, et al., Phys. Lett. B 614 (2005) 174.
- [34] Z. Dombradi, et al., Phys. Lett. B 621 (2005) 81.
- [35] H. J. Ong, et al., Phys. Rev. C 73 (2006) 024610.
- [36] S. Michimasa, et al., Phys. Lett. B 638 (2006) 146.
- [37] Z. Elekes, et al., Phys. Rev. C 74 (2006) 017306.
- [38] Z. Elekes, et al., Phys. Rev. C 73 (2006) 044314.
- [39] Z. Dombradi, et al., Phys. Rev. Lett. 96 (2006) 182501.
- [40] J. Gibelin, et al., Phys. Rev. C 75 (2007) 057306.
- [41] D. Suzuki, et al., Phys. Lett. B 666 (2008) 222.
- [42] H. J. Ong, et al., Phys. Rev. C 78 (2008) 014308.
- [43] H. Iwasaki, et al., Phys. Rev. C 78 (2008) 021304.
- [44] Z. Elekes, et al., Phys. Rev. C 79 (2009) 011302.
- [45] N. Aoi, et al., Phys. Rev. Lett. 102 (2009) 012502.
- [46] S. Takeuchi, et al., Phys. Rev. C 79 (2009) 054319.
- [47] P. Doornenbal, et al., Phys. Rev. Lett. 103 (2009) 032501.
- [48] P. Doornenbal, et al., Phys. Rev. C 81 (2010) 041305.
- [49] Z. Elekes, et al., Phys. Rev. C 82 (2010) 027305.
- [50] Y. Togano, et al., Phys. Rev. Lett. 108 (2012) 222501.
- [51] K. A. Li, et al., Chin. Phys. Lett. 29 (2012) 102301.
- [52] S. Takeuchi, et al., Phys. Rev. Lett. 109 (2012) 182501.
- [53] H. Suzuki, et al., Phys. Rev. C 88 (2013) 024326.
- [54] D. Steppenbeck, et al., Nature(London) 502 (2013) 207.
- [55] P. Doornenbal, et al., Phys. Rev. Lett. 111 (2013) 212502.
- [56] S. Takeuchi, et al., RIKEN Accel. Prog. Rep. 36 (2003) 148.
- [57] The DALI2 website, <http://www.nishina.riken.jp/collaboration/SUNFLOWER>.
- [58] H. Ryuto, et al., Nucl. Instrum. Methods Phys. Res. Sect. A 590 (2008) 204.
- [59] Y. Mizoi, et al., RIKEN Accel. Prog. Rep. 38 (2005) 297.
- [60] Saint-Gobain Crystals website, <http://www.detectors.saint-gobain.com>.
- [61] SCIONIX Holland BV, P.O.Box 143, CC Bunnik, The Netherlands.
- [62] Hamamatsu Photonics K.K., <http://www.hamamatsu.com/jp/ja/index.html>.
- [63] CAEN S.p.A, <http://www.caen.it>.
- [64] H. Baba, et al., Nucl. Instrum. Methods Phys. Res. Sect. A 616 (2010) 65.
- [65] R. Anhold, et al., Phys. Rev. Lett. 53 (1984) 234.
- [66] R. Anhold, et al., Phys. Rev. A 33 (1986) 2270.
- [67] R. Holzmann, et al., GSI Annual Report 1992 (1993) 48.
- [68] GEANT3, CERN Program Library Long Writeup W5013, [http://wwwasdoc.web.cern.ch/wwwasdoc/geant\\_html3/geantall.html](http://wwwasdoc.web.cern.ch/wwwasdoc/geant_html3/geantall.html), 1993.
- [69] G. F. Knoll, Radiation Detection and Measurement, Wiley, New York, 1979. and references there in.
- [70] W. R. Leo, Techniques for Nuclear and Particle Physics Experiments, Springer-Verlag, Berlin, 1994. and references there in.
- [71] J. Raynal, coupled-channel code ECIS97 (unpublished).
- [72] The SHOGUN website, <http://www.nishina.riken.jp/collaboration/SUNFLOWER>.
- [73] P. Doornenbal, et al., RIKEN Accel. Prog. Rep. 42 (2009) 182.
- [74] E. Farnea, et al., Nucl. Instrum. Methods Phys. Res., Sect. A 621 (2010) 331.
- [75] K. Yoneda, et al., RIKEN Accel. Prog. Rep. 45 (2012) i.
- [76] T. Uesaka, et al., Nucl. Instrum. Methods Phys. Res., Sect. B 266 (2008)

4218.